A new method for the characterization of temperature dependent thermo-physical properties

T.R. Pavlov[a,b,*], D. Staicu[a], L. Vlahovic[a], R.J.M. Konings[a], P. Van Uffelen[a], M.R. Wenman[b]

[a] European Commission, Joint Research Centre, Institute for Transuranium Elements, P.O. Box 2340, 76125 Karlsruhe, Germany
[b] Centre for Nuclear Engineering, Imperial College London, Royal School of Mines, London, SW7 2AZ England, United Kingdom

ABSTRACT

The proposed method is based on the laser flash technique. Radially distributed thermograms are calculated via a finite element model and used in an inverse method by optimizing either specific heat or thermal conductivity of a material. These properties are evaluated as a function of radius and respective temperature. Two approximations are introduced inferring the dependence of each property as a function of radius – a polynomial (PNOM) approximation and an iterative gradient (IG) approximation. The method was tested using synthetic thermograms and both approximations were capable of yielding excellent results. The IG approximation was more universal and less sensitive to initial fitting parameters. The PNOM approximation was less computationally expensive but was prone to artefacts (such as un-physical minima or maxima) and more dependent on initial fitting parameters. Both approximations were successfully used on experimental data from UO_2 and isostatically pressed graphite. Thermal conductivity was within 5% of the reference empirical correlation for UO_2 and within 7% of the reference curve for graphite.

1. Introduction

The growing need for the determination of thermo-physical properties of materials has prompted the development of innovative techniques. One of these techniques is the laser flash method. The original method was developed by Parker, in which he used a flash lamp to produce a heat pulse traveling from the front to the rear surface of a specimen. By modelling the heat transfer conditions of the experiment, he was able to obtain an expression for thermal diffusivity [1]. His analytical solution assumed an instantaneous surface heat source, sample opacity, only axial heat conduction and no heat losses. Cowan's solution [2] introduced radiative heat losses, while Ronchi et al. also considered the radial conduction of heat [3] and determined simultaneously thermal diffusivity, specific heat capacity and hence thermal conductivity by least squares fitting between model and experimental data. Recently, a finite element model was developed by Pavlov et al. [4] incorporating the measured spatial profile of the laser beam. Other works made use of spatially resolved infrared thermography in order to evaluate the thermal diffusivity of a material [5–7]. However, the adopted analytical solutions either neglected heat losses [8] or considered one-dimensional heat flow [6,7]. So far all methods evaluate a single value of a thermal property from a single measurement. Furthermore, all of the above models assume the temperature, and hence properties, throughout the sample to be constant.

In this work an improved method is described by extending the previously developed inverse method [4] to evaluate either thermal conductivity or specific heat capacity as a function of radius, and hence, temperature. In order to achieve this goal, the numerical model will be coupled with the measurements obtained from an infrared camera. This coupling allows the determination of temperature dependent curves, of the aforementioned properties, with a single laser flash measurement. Hence, the method offers a means of measuring thermal conductivity or specific heat capacity as a function of temperature (i.e. an entire temperature dependent profile) with a single measurement. Furthermore, in a future study the method's capability of evaluating the properties of radially heterogeneous materials could be tested. An example of such systems is irradiated nuclear fuel [9,10], whereby the microstructure and composition of the material varies strongly with respect to the fuel pellet radius. However, spatial heterogeneity is not the subject of the current study. This work is focused on introducing the new method, testing its theoretical capability of retrieving the intrinsic, i.e. correct or exact, temperature dependent profile of either specific heat or thermal conductivity (using synthetic or computer generated data) and finally testing the methodology with real experimental data.

* Corresponding author.
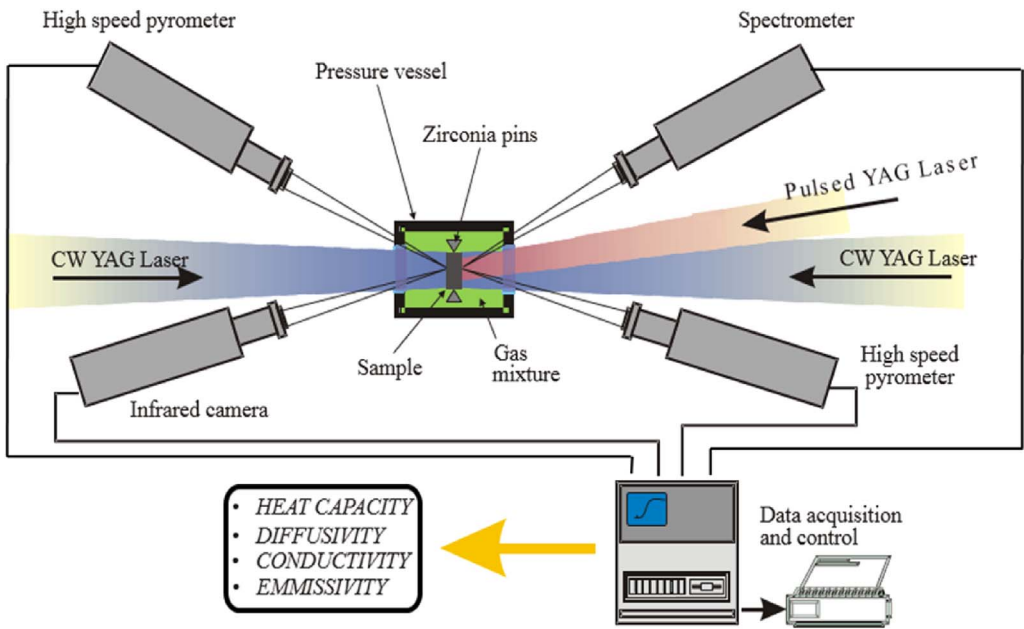 E-mail address: tsvetoslav.pavlov09@imperial.ac.uk (T.R. Pavlov).

Fig. 1. Schematic of experimental set-up representing a modified version of a diagram published previously [4].
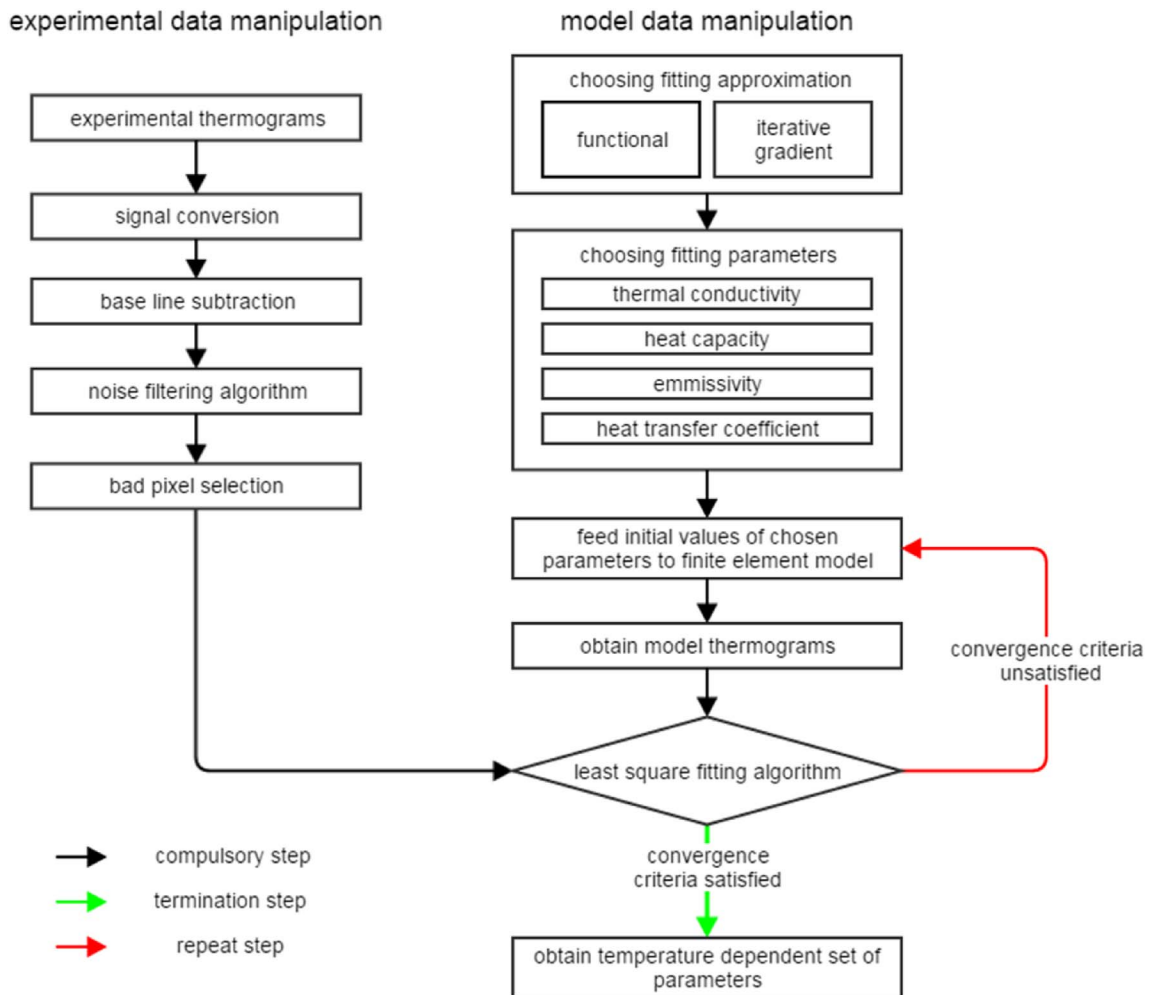

Fig. 2. Logic diagram of the inverse method program.

2. Methodology

2.1. Laser flash experiment

Fig. 1 shows the schematic of the laser flash equipment. A disc shaped sample is held by three or four zirconia pins to a graphite sample holder. These are placed in a chamber or steel vessel of controlled atmosphere of argon at a pressure of 4 bar. Prior to filling the buffer gas, the chamber is flushed. The flushing is performed by filling and subsequently pumping out a mixture of Ar-5%H_2 (vacuum is limited to 5 μbar). This is done to reduce the residual moisture content. The maximum temperature of the steel vessel during the experiment has been estimated to be of the order of 325 K. The chamber has two sapphire windows, through which two continuous-wave lasers (Nd-YAG with λ = 1064 nm produced by TRUMPF and Haas Laser GmbH) preheat each side of the specimen from around 300 K to a chosen equilibrium temperature. The laser spots are aligned at the centre of the sample surfaces. The equilibrium temperatures are usually varied from around 1000 K to above 3000 K. The temperatures are continuously monitored by high speed pyrometers on the front and rear sides. Furthermore, a spectropyrometer measures the radiance on the front side at 256 wavelengths in the range of 500–1000 nm and is used for evaluating the spectral emissivity of the sample [4]. The acquisition time of the spectropyrometer can range from 40 ms to 1 s, depending on the temperature measured and a maximum of 256 time frames can be recorded in a single measurement. The acquisition time used for the high speed pyrometers can be as low as 500 ns (50 μs is typically used) and the recorded time interval typically consists of at least 70000 time frames. The relative error on the temperature measurement is less than 2% (inclusive of the error arising from the uncertainty of the measured emissivity). The focal distances of the high speed pyrometers are 381 ± 5 mm and 450 ± 5 mm, respectively, while the focal length of the spectropyrometer is 440 ± 5 mm.

Once a steady state has been obtained, a short laser pulse is applied (generally between 1 ms and 10 ms) by ramping up and then down the power of the front laser. On the rear side the rise in temperature is measured as a function of time via a Phoenix infrared camera with a very narrow band pass filter centred at 1600 nm, which is automatically triggered upon the initiation of the laser pulse. A set of radially distributed thermograms is then recorded and transferred directly to a personal computer (PC). The thermal camera (with the narrow band pass filter) was calibrated by the Laboratoire national de métrologie et d'essais for a temperature range of 900 K–3200 K without the sapphire window. The transmissivity of the sapphire window has been estimated at JRC Karlsruhe to be 0.86 ± 0.03. All pixels have been corrected for non-uniformity via a two point correction. The acquisition time of the thermal camera is 200 μs and 4000 time frames are recorded during each measurement. The focal length of the camera is 600 mm. The camera, lasers and pyrometers are positioned at angles no greater than 5° to the normal of the plane parallel to the sample surface.

The pyrometer measurements are transferred to a 14-bit digitiser (Nicolet Pro 34) and then stored on a PC. Finally, all recorded radiance signals are converted into an actual temperature reading, using the spectral emissivity estimated by the spectropyrometer. (It is worth noting that the wavelength of operation of the camera is above the upper limit of the spectropyrometer. For the current samples, i.e. UO_2
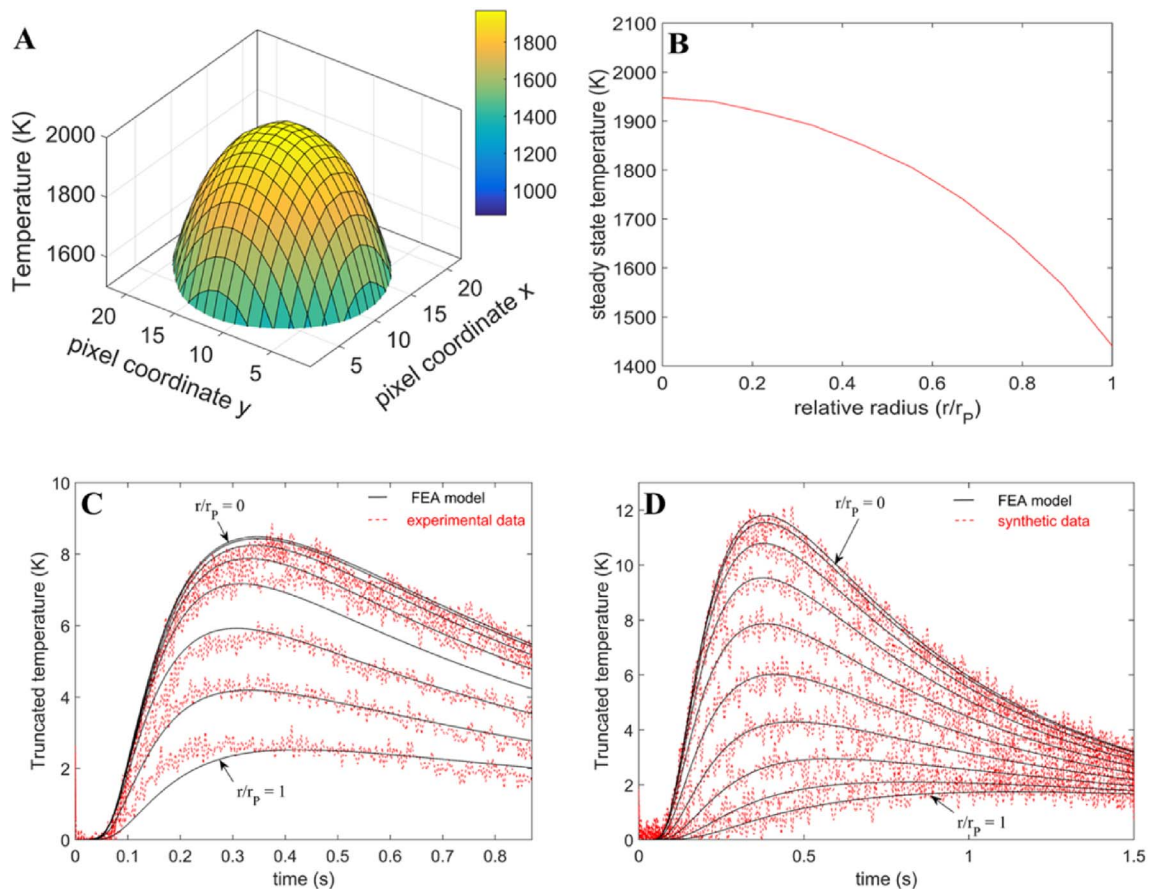

Fig. 3. Steady state and transient measurements recorded using an infrared camera. (A) example of a 3D steady state temperature profile of a UO_2 sample. The magnitudes of the x and y axes are indices and not metric quantities.; (B) the axisymmetric steady state temperature distribution deduced from (A); (C) example of radially distributed thermograms for a UO_2 sample measured by the infrared camera compared to the optimised finite element (FEA) solution. (D) radially distributed synthetic thermograms (produced via the FEA model with perturbed input parameters and added artificial noise) compared to the optimised finite element solution.

and isostatically pressed graphite, there is available literature data showing the invariance of emissivity within an extended wavelength range. However, in other cases spectral emissivity may vary strongly as a function of wavelength. Hence, an additional device or method would necessary for determining spectral emissivity at 1600 nm).

2.2. Fitting procedure

A logic diagram of the method is shown in Fig. 2. The experimental thermograms are converted from a signal reading to a temperature reading. Prior to the onset of the laser pulse, the base lines of the radially distributed pixels are recorded. This provides the information for a base line correction. Furthermore, for noisy data fast Fourier transforms have been employed to filter the noisy data. The detailed description of the filtering approach has been described in detail in a previous study [4]. Additionally, bad pixels (defective pixels constrained to the maximum signal value, to which the signal of a neighbouring pixel is assigned) in the camera can be detected and omitted during the fitting stage.

The model thermograms are calculated via a finite element analysis (FEA) model created with FlexPDE [11] (more details in section 2.4) and are then fitted to experimental data using one of two approximations - a functional and an iterative gradient (IG) approximation. Figs. 3A, 3B and 3C show the typical steady state and transient profiles obtained from the infrared camera. Furthermore Figs. 3C and 3D show the converged transient model results compared to experimental data as well as simulated data (with added white noise and an input parameter peturbation of 0.5%).

2.3. Fitting approximations

Two approximations are used to model the radially distributed thermograms obtained experimentally – a functional approximation and an iterative gradient (IG) approximation. The functional approximation pre-sets an equation based radial dependence (and hence temperature dependence) on the calculated properties. The parameters describing the property's function are then optimised. In this study, a polynomial function is used to approximate the property variation as a function of radius and hence this approximation is referred to as the PNOM approximation. The respective fitting parameters are the N

number of constants describing a polynomial of order N-1, which can be seen from equation (1). In equation (1) thermal conductivity ($k(r)$) serves as an example property; the method can be applied to multiple properties such as thermal conductivity, specific heat capacity and possibly total hemispherical emissivity. Throughout the rest of this work a 2nd order polynomial will be used, which is described by 3 constants (a_0, a_1, a_2), i.e. fitting parameters.

$$k(r) = \sum_{i=1}^{N} a_{i-1} r^{i-1} \tag{1}$$

The IG approximation does not assume a global functional form for the radial dependence (and hence temperature dependence) of the calculated property. Using this approach the central thermal conductivity is calculated first and stored at its respective position, while the neighbouring value is allowed to fluctuate and thus establish a linear gradient between the two radial positions. The calculated properties are stored and the iteration process moves in a radial direction from the centre towards the outer edge.

Fig. 4 shows a schematic of the IG approximation. The first iteration assumes constant properties along the sample radius, which is a sufficiently good approximation for a relatively large (in terms of surface area) and homogenous surface heat source. The obtained values (e.g. $k(r_1)$) in the first iteration are stored and are invariant within the first radial segment (first small section of the rectangular box in Fig. 4) during iteration 2. It must be noted that the first radial segment is made infinitesimally small, confining the converged property value to $r_1 = 0$ (e.g. $k(r = 0)$). During iteration 2 a linear gradient is established to describe the local property variation as a function of radius. By using the stored properties from the previous iteration ($k(r_{stored})$ in equation (2)) only one parameter is varied, namely the gradient of the line (e.g. m_2 or equivalently $\frac{dk}{dr}\big|_{r=r_2}$ in equation (2)). At a critical radius (r_c) the linearly varying property becomes radially invariant. Hence, a step function is achieved with a cut-off radius at r_c. Upon convergence the linear variation of the properties is stored within the second radial segment and the process moves on towards the edge of the axisymmetric geometry. Another way to imagine this procedure is via a first order Taylor expansion:
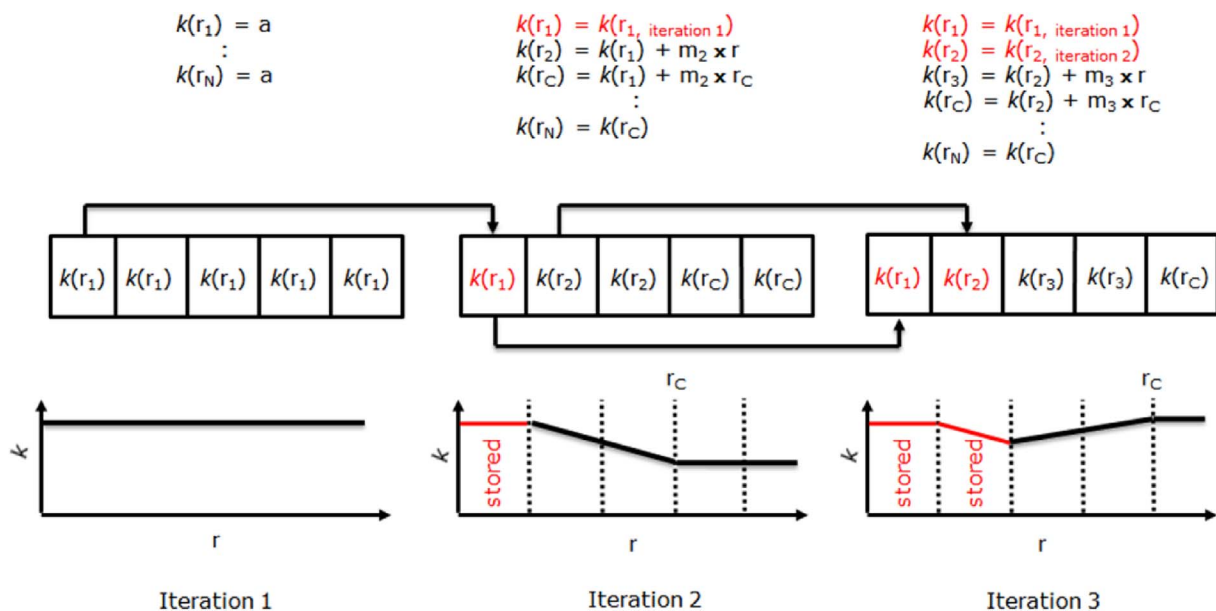

Fig. 4. Schematic of the first three iterations of the iterative gradient approximation. In black are all the values, which are allowed to vary during the optimization procedure of the respective iteration, while in red are the values which have been stored and fixed as a result of prior iterations. (For interpretation of the references to colour in this figure legend, the reader is referred to the web version of this article.)

$$k(r)_i \approx \begin{cases} k(r_{stored}) & r \in \{0, \ r_{i-1}\} \\ \left\{ k(r_{i-1}) - r_{i-1}\frac{dk}{dr}\Big|_{r=r_i} \right\} + r\frac{dk}{dr}\Big|_{r=r_i} & r \in \{r_{i-1}, \ r_C\} \\ \left\{ k(r_{i-1}) - r_{i-1}\frac{dk}{dr}\Big|_{r=r_i} \right\} + r_C\frac{dk}{dr}\Big|_{r=r_i} & r \in \{r_C, \ r_P\} \end{cases} \tag{2}$$

where i represents the respective iteration and also coincides with the radial segment identifier (e.g. r_1, r_2, etc.).

2.4. Finite element analysis (FEA)

The FEA model, which has been created with the FlexPDE [11] software, is axisymmetric. The model describes the transient conditions in the sample immediately after the onset of the laser pulse.

The governing equation is the transient heat equation:

$$\rho(r)C_p(r)\frac{\partial T}{\partial t} = \nabla \cdot (k(r, T_0)\nabla T) \tag{3}$$

where ρ is the density (kg m^{-3}), C_p is the specific heat capacity (J kg^{-1} K^{-1})), k is thermal conductivity (J s^{-1} m^{-1} K^{-1}), T is temperature (K) and t is time (s). Thermal conductivity ($k(r, T_0)$) is defined in a more general mathematical form as both space and temperature dependent. However for the systems considered in the current work this property is purely temperature dependent, as the investigated materials are spatially homogeneous and isotropic.

Furthermore, a reduced variable is introduced such that:

$$T(t, r, z) = T(0, r, z) + \Psi(t, r, z) = T_0 + \Psi \tag{4}$$

where T_0 is the steady state temperature (K) and Ψ is the reduced variable temperature (K). The reduced variable is needed so that only the transient part of the experiment is simulated. This allows for the experimental steady state profile to be used as input and not simulated. The experimental steady state temperatures, at a particular radial position, are then the temperatures corresponding to the evaluated property at that same radial location. Based on the reduced variable (reduced temperature), the reduced (Neumann) boundary conditions expressing the heat balance on the surfaces are:

$$-k(r, T_0)\frac{\partial \Psi}{\partial z}\Big|_{z=0} = \theta(r, t) \times \varepsilon_{1064} - h(T) \times [T - T_0]$$
$$- \varepsilon_{tot}(T) \times \sigma \times [T^4 - T_0^4] \tag{5}$$

$$-k(r, T_0)\frac{\partial \Psi}{\partial z}\Big|_{z=z_{sample}} = -h(T) \times [T - T_0] - \varepsilon_{tot}(T) \times \sigma \times [T^4 - T_0^4] \tag{6}$$

$$-k(r, T_0)\frac{\partial \Psi}{\partial r}\Big|_{r=r_{sample}} = -h(T) \times [T - T_0] - \varepsilon_{tot}(T) \times \sigma \times [T^4 - T_0^4] \tag{7}$$

where $h(T)$ is the temperature dependent convective heat transfer coefficient (W m^{-2} K^{-1}) and determines the amount of heat lost due to natural convection (details on the calculation of this property have been provided in a previous study [4]), ε_{tot} is the total hemispherical emissivity, which is related to the heat lost due to radiation and $\varepsilon_{(1064\ nm)}$ is the emissivity at the laser wavelength (absorptivity) and represents the fraction of laser light absorbed by the sample, z_{sample} is the specimen thickness (m) and r_{sample} is the sample radius (m). Finally, the left hand side of equations (5)–(7) represents the heat flux transferred from the sample surface to the bulk (also known as Fourier's law).

In accordance with equation (4), the initial condition is:

$$\Psi_{t=0} = 0 \tag{8}$$

The properties of the graphite and UO$_2$ samples used, together with the corresponding laser parameters, are tabulated in Table 1 and Table 2. The relative convergence criteria used for the temperature calculation performed by the FEA model is 0.2%. Quadratic triangular

Table 1
Summary of sample characteristics and laser beam parameters.

Material	Parameter (units)	Value range
UO$_2$	room temperature density ρ_{273} (kg m^{-3})	10200
	porosity (%)	7
	thickness (mm)	0.9
	radius (mm)	4.175
	beam spot radius (mm)	2.5
	pulse duration (ms)	10
graphite	room temperature density ρ_{273} (kg m^{-3})	1810
	porosity (%)	20
	thickness (mm)	3.05
	radius (mm)	2.495
	beam spot radius (mm)	1.5
	pulse duration (ms)	10

mesh elements (6 nodes per element) have been used. Adaptive re-meshing has been used starting from a mesh with 30 grid points alongside the larger dimension and a proportional number of grid points alongside the smaller dimension. This number of grid points has been determined in order for the numerical error of the variables to converge with respect to the initial mesh density and be lower than 0.2%. The time step is automatically adjusted by FlexPDE as for the cubic term in a Taylor expansion of the variables in time to be lower than the convergence criteria applied (0.2%) [11]. Finally, the energy density of the laser pulse in equation (5) is described by the following relationship:

$$\theta = \frac{P(r, t)}{\pi r_b^2} \tag{9}$$

where P (J s^{-1}) is the power of the laser pulse, θ is the power density (J s^{-1} m^{-2}) deposited by the beam, r_b is the waist or beam spot radius (m).

2.5. Optimization algorithm

The Levenberg-Marquardt method [18,19] was used to find the least square minimum between the experimental thermograms and the model thermograms. The convergence criterion used is the relative difference in the parameter vector between two consecutive iterations. If this absolute relative difference is lower than 10^{-4} after two consecutive parameter updates, the code terminates. The other convergence criterion is related to the gradient of the least square difference between model and experimental thermograms (see equation (12)) and is discussed below. The method has been designed to work with four types of fitted parameters, namely, thermal conductivity (k), specific heat capacity (C_p) heat transfer coefficient (h) and total hemispherical emissivity (ε_{tot}). Thermal diffusivity can also be identified (as suggested in Fig. 1), indirectly from the other fitted properties. This means that if for instance the code is used to evaluate thermal conductivity, then by using the obtained results, in addition to literature values for specific heat and density, one can calculate thermal diffusivity:

$$p = \begin{pmatrix} k \\ c_p \\ h \\ \varepsilon_{tot} \end{pmatrix} \tag{10}$$

The parameters in equation (10) can be scalars or vectors (e.g. several parameters per property describing a polynomial functional form of the property). It is also important to note that due to the correlation results shown in section 3.1, the proposed methodology in this work can only estimate one property at a time (out of the four given by equation (10)). The other properties then must be provided as input. The cost function (f_c) for the least square minimisation is the following:

Table 2
Material properties of UO₂ and isostatically pressed graphite used as input in the FEA model.

Material	Property	Expression	Reference
UO₂	$\rho(T)$	$\rho_{273}\{9.973 \times 10^{-1} + 9.08 \times 10^{-6}\,T - 2.705 \times 10^{-6}T^2 + 4.391 \times 10^{-13}T^3\}$	[12]
	$\varepsilon_{(1064\ nm)}$	0.9	[13]
	$\varepsilon_{(1600\ nm)}$	$0.836 + 4.321 \times 10^{-6}(T - 3120)$	[14]
	ε_{tot}	0.85	[15]
graphite	$\rho(T)$	$\rho_{273} \times (5 \times 10^{-13}\,T^3 - 8 \times 10^{-10}T^2 + 6 \times 10^{-6}T + 0.9981)$	[16]
	$\varepsilon_{(1064\ nm)}$	$4.053156 \times 10^{-5}T + 0.8739063$	[16]
	$\varepsilon_{(1600\ nm)}$	0.87	[4]
	ε_{tot}	$0.92 - 5.33 \times 10^{-6}T$	[17]

$$f_c(p) = \sum_{i=1}^{N} (f_M(p, t_i) - f_E(t_i))^2 \qquad (11)$$

$$\frac{df_c}{dp} < 10^{-4} \qquad (12)$$

where f_M is the time dependent temperature profile calculated by the model, f_E is the time dependent temperature profile measured by the infrared camera, t_i is the time at which a temperature reading was recorded by the camera, after initiation of the laser pulse, i is the index of the temperature measurement at a particular time and N is the total number of temperature records acquired at different times t_i.

3. Results and discussion

3.1. Sensitivity analysis and parameter correlation

The method presented in this paper can have a set of fitted (output) parameters as well as various input parameters. It is important to understand how each of these parameters affects the model thermograms, in order to: 1) asses the relative importance of input and fitting parameters 2) examine the interdependence between parameters. As a first step the sensitivity coefficients (S_i) are calculated for each parameter:

$$S_i(t) = \frac{df(t)}{dp_i} p_i \qquad (13)$$

where $f(t)$ is the model thermogram (K), p_i is the respective parameter and t is time (s). The sensitivity curves for all parameters are shown in the Appendix. Fig. 5 shows the integral sensitivity coefficients according to equation (14). All derivatives and integrals have been performed numerically using the forward difference method and trapezoidal rule, respectively.

$$\int S_i(t) = \int_{0}^{1.5} \left| \frac{df(t)}{dp_i} p_i \right| dt \qquad (14)$$

where the limits of the integral represent the duration of the transient (thermogram), i.e. a duration of 1.5 s. A high value of $S_i(t)$ indicates high sensitivity. Parameters with larger sensitivity (or also integral sensitivity) coefficients have relatively larger influence on the output compared to parameters with lower $S_i(t)$ values. Fig. 5 shows a general nonlinear drop in the sensitivity of all parameters towards the edge of the sample. This follows the radial drop in the deposited laser energy density from the centre of the sample towards the outer periphery. This could lead to experimental disturbances (e.g. noise) having an
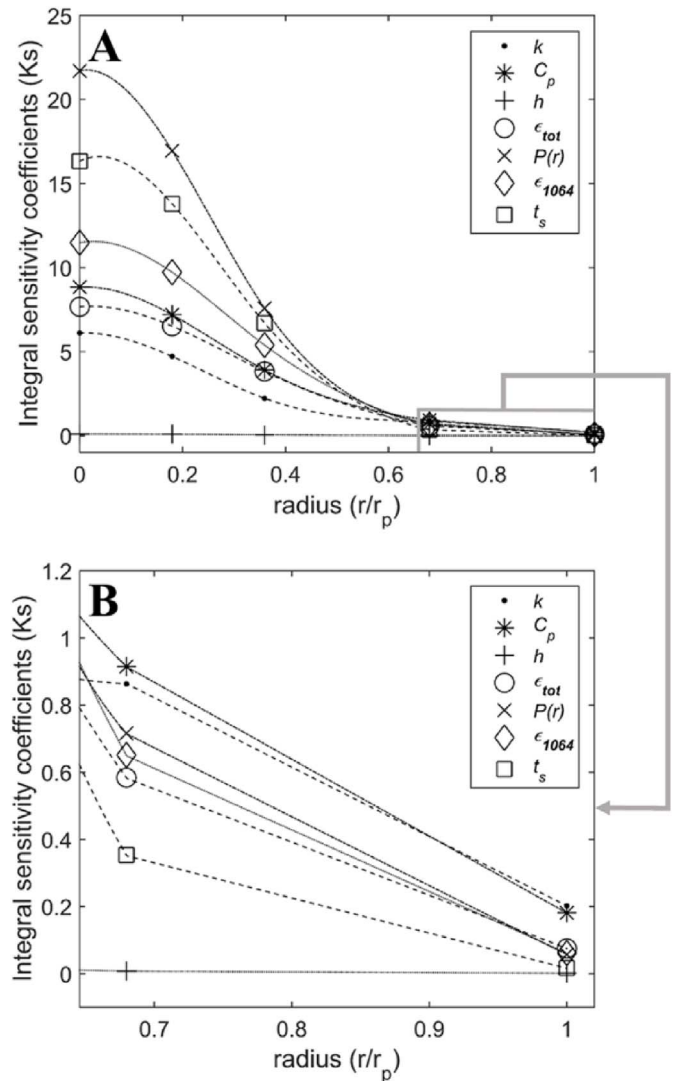

Fig. 5. Integral sensitivity coefficients vs normalised radius (r/r_p) for the potential fitting parameters - thermal conductivity (k), specific heat (C_p), convective heat transfer coefficient (h) and total hemispherical emissivity (ε_{tot}), as well as the input parameters – spatial laser power profile ($P(r)$), normal spectral emissivity at 1064 nm (ε_{1064}), sample thickness (t_s). These have been obtained by applying equation (13) to the results presented in Figure A1 (see Appendix); (B) Zoom-in of the lower right corner of (A).
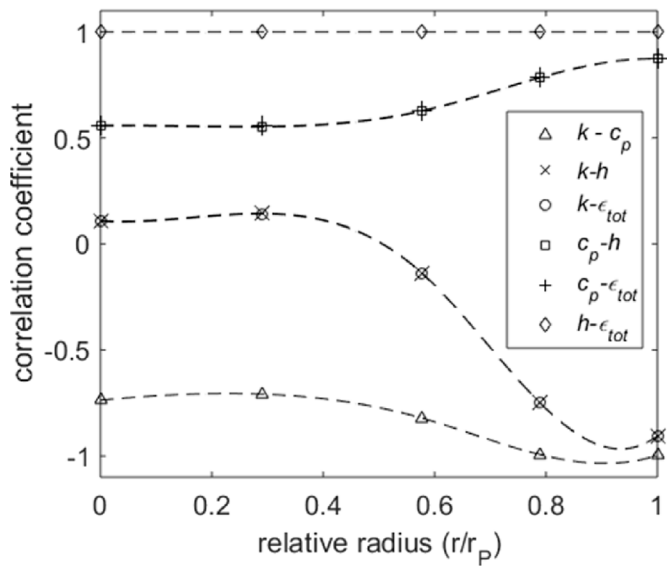
Fig. 6. The correlation "Pearson" coefficient of parameter pairs vs. relative radial position. The chosen parameters are based on equation (10) and are thermal conductivity (k), specific heat (C_p), convective heat transfer coefficient (h) and total hemispherical emissivity (ϵ_{tot}). The numerical values of the correlation coefficients for each parameter pair can be found in Tables A1 to A5 (see Appendix).

increasingly stronger adverse effect on the accuracy of the property values towards the sample periphery. However, this negative effect could be partially offset by the increase in the relative integral sensitivity of the parameters of interest, namely thermal conductivity and specific heat capacity. Fig. 5 shows thermal conductivity and specific heat capacity become the most sensitive parameters at $r/r_p = 1$.

An important way to analyse the potential and also the limitations of the proposed methodology is to look at the interdependence of parameters and in particular the Pearson correlation coefficient is used to do this. This parameter can be calculated in the following manner:

$$\rho_{ij} = \frac{\int_0^{t_D} \left(\frac{df(t)}{dp_i} \cdot \frac{df(t)}{dp_j} \right) dt}{\left[\left(\int_0^{t_D} \left(\frac{df(t)}{dp_i} \right)^2 dt \right) \cdot \left(\int_0^{t_D} \left(\frac{df(t)}{dp_j} \right)^2 dt \right) \right]^{1/2}}$$

(15)

where ρ_{ij} is the correlation coefficient between parameters i and j. By calculating the coefficient for each pair in the parameter vector (refer to equation (10)), it can be determined which pairs of parameters may be suitable for simultaneous determination. Highly correlated parameters, with their absolute correlation coefficients (positive or negative) approaching unity, are not suitable for simultaneous fitting as it is easy to obtain good fits (low least squares difference between model and experimental data) with a set of physically unsound parameter values. Hence, the inverse problem becomes highly ill-posed.

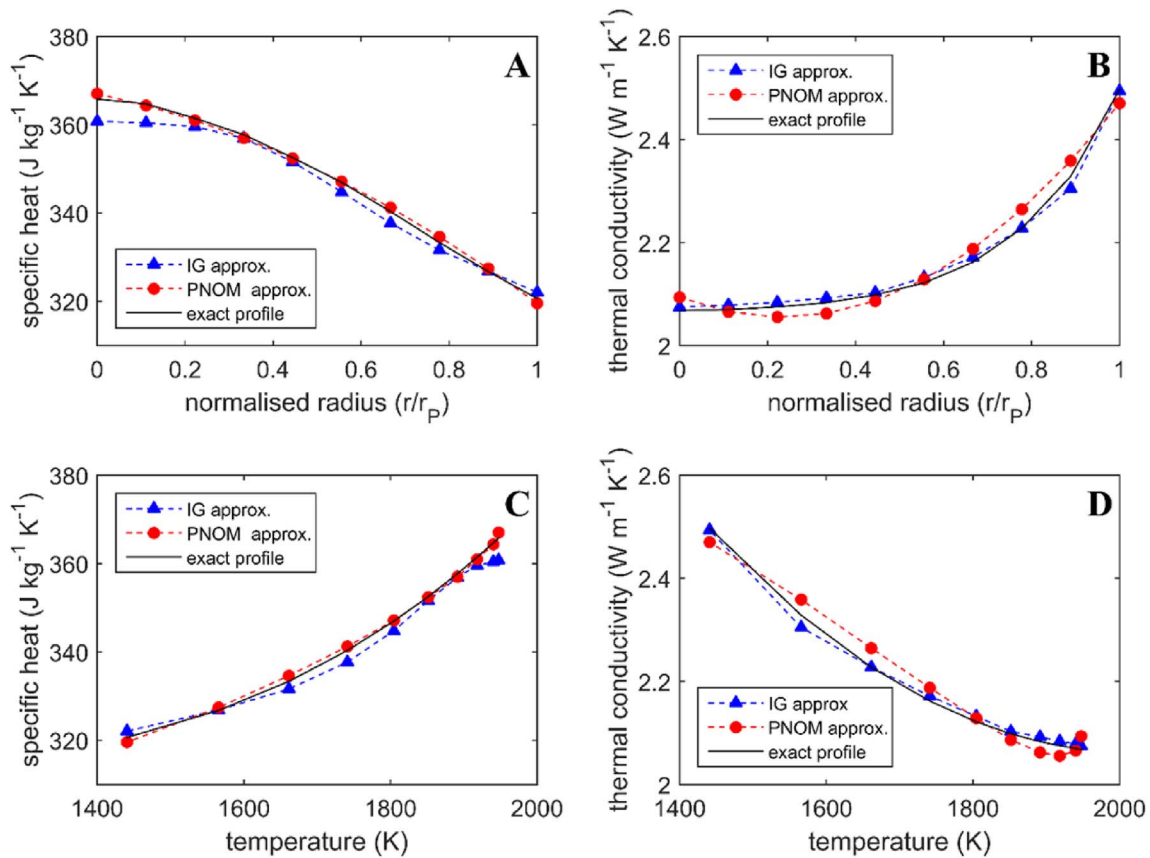In Fig. 6 the correlation curves for 6 unique pairs of fitting

Fig. 7. Graph A shows specific heat vs. normalised radius. Graph B shows thermal conductivity vs. normalised radius. Both plots compare the output of the two approximations (Iterative gradient (IG) approximation vs. polynomial (PNOM) approximation) to the exact solution (the exact solutions are the property profiles used to generate the synthetic thermograms, which were then used to test the approximations). The two property profiles were obtained from independent runs of the IG and PNOM approximations (i.e. the two properties were not fitted simultaneously). Graph C shows specific heat vs. temperature. Graph D shows thermal conductivity vs. temperature. Graphs C and D were obtained by assigning the known temperature at each radial position to the corresponding property value at the same radial coordinate.

parameters are shown (based on the parameters in equation (10)). The correlation coefficients have been plotted as a function of radius in order to examine the radial dependence between parameters. This is done, in order to understand if simultaneous property determination is possible for all radially distributed thermograms. In Fig. 6 it is evident that the heat loss parameters heat transfer coefficient (h) and total hemispherical emissivity (ε_{tot}) are very strongly positively correlated and hence cannot be fitted simultaneously. Furthermore, all parameter pairs tend to become strongly correlated towards the edge of the sample, making simultaneous fitting inadvisable. However, simultaneous fitting of thermal conductivity, specific heat capacity and one of the heat loss parameters (preferably total hemispherical emissivity due to the significantly larger sensitivity) is possible for the central thermogram. This has been already investigated by Pavlov et al. [4] and Ronchi et al. [3]. Hence, using the current methodology one should investigate the radial profile of one property at a time, in order to improve the well-posedness of the inverse problem.

3.2. Synthetic data tests

In order to assess the two approximations (IG approximation and PNOM approximation), a set of synthetic thermograms were created based on the thermophysical properties of UO_2, a material which has been widely studied in literature [12]. Most of these properties are listed in Tables 1 and 2. The input parameters – steady state radial temperature profile of the sample, sample dimensions and laser beam spot characteristics, are obtained experimentally, based on a laser heating experiment (Fig. 1) performed on a UO_2 specimen. The reference thermal conductivity used was taken from Ronchi et al. [3], while the reference specific heat capacity was taken from Fink et al. [12]. The functions of these properties can be found in the Appendix (equations A1 and A2).

Once, the synthetic thermograms are calculated, each approximation is initiated away from the optimal parameters describing the intrinsic or exact profile of a property– either specific heat capacity or thermal conductivity. As it was shown in the previous section, it is important to fit only one property and its associated parameters at a time. Fig. 7 compares the two approximations and their solutions to the exact solution (input property for producing synthetic data). Separate evaluations were completed for thermal conductivity and specific heat capacity.

Fig. 7 clearly shows that both approximations yield results, which are representative of the exact solutions. The IG approximation outperforms the PNOM approximation in the case of thermal conductivity, while the PNOM approximation gives a slightly better estimate of the specific heat capacity profile. This can also be shown by comparing the relative standard deviation (RSD) and R^2 values of each approximation for the two properties (based on equations (16)–(18)). In the case of specific heat capacity the PNOM output exhibits both a lower RSD, as well as higher coefficient of dependence (R^2), while for thermal conductivity the output of the IG approach is associated with both a lower RSD and higher R^2.

Table 3

Comparison of the relative standard deviation (RSD) and the coefficient of determination (R^2) for the output of each approximation.

Statistical parameter	IG	PNOM
RSD of C_p (%)	0.23	0.07
RSD of k (%)	0.15	0.34
R^2 of C_p	0.967	0.997
R^2 of k	0.993	0.971

$$R^2 = 1 - \sum_i^N \frac{(f_{exact}(r_i) - f_{evaluated}(r_i))^2}{(f_{exact}(r_i) - \overline{f}_{evaluated})^2} \tag{16}$$

$$RSD = \frac{1}{\overline{f}_{exact}} \sum_i^N \frac{\sqrt{(f_{exact}(r_i) - f_{evaluated}(r_i))^2}}{N-1} \tag{17}$$

$$\overline{f}_{exact} = \sum_i^N \frac{f_{evaluated}(r_i)}{N} \tag{18}$$

where f_{exact} is the exact profile of the property, $f_{evaluated}$ is the evaluated profile of the property using either the PNOM or IG approximation, $\overline{f}_{exact}$ is the mean of the exact property profile (see Table 3).

The radial profile of thermal conductivity cannot be very exactly reproduced by a 2nd order polynomial and hence the PNOM approximation performs worse. Furthermore, the polynomial can yield unphysical phenomena such as pronounced minima or maxima, while in reality this is just a functional-fitting artefact. This can be observed in Fig. 7B and 7D where the PNOM approximation erroneously predicts a minimum in thermal conductivity at $r/r_p \approx 0.25$ at around 1925 K. In terms of computation time the IG approximation is more expensive and scales linearly with the number of radially distributed thermograms. The IG approximation was initialised around 64% away from the exact profile (for thermal conductivity at 3.4 W m^{-1} K^{-1} while for specific heat at around 600 J kg^{-1} K^{-1}). The PNOM approximation was initialised with parameter values only 15% away from the values representing the optimal fit to the exact profile as the PNOM approximation is more sensitive to the initial values of its parameter vector. Hence, in cases where the temperature dependence of the evaluated property is completely unknown, the converged parameter set may not accurately reflect the true underlying property profile. The IG approach is less sensitive to the initial values as it fits a single parameter per property at a time. This makes the IG approximation very attractive when there is no prior knowledge of the temperature dependence of a property. Hence, the IG approach is more general and non-parametric in nature.

3.3. Tests with experimental data

Ultimately, the capabilities of the newly developed methodology and its coupling with the laser flash set-up (described in Section 2.1) were tested. Two different materials were investigated and their thermal conductivities were evaluated. These materials were UO_2 and isostatically pressed polycrystalline graphite. The results of their thermal conductivities are presented in Fig. 8. It is clear that the PNOM approximation and the IG approximation yield good results for both materials. The UO_2 results were corrected to 95% porosity using the Brand and Neuer correction [20]. The model curve in Fig. 8B is representative of the experimental data in this temperature range, as has been previously shown by Pavlov et al. [4]. The error on thermal conductivity is 19.6% based on a 3-level full factorial design described in detail in a previous study [4]. It must be noted, however that the relative error has been assumed independent of the radial location at which the property has been evaluated. This assumption will be assessed in a future study.

Fig. 8 shows rather flat thermal conductivity profiles with respect to temperature for both materials. In the case of graphite, this is due to its high thermal conductivity. Hence, the gradient in temperature across the sample radius is small and the thermal conductivity could only be evaluated in a small temperature range as shown in Fig. 8B. Uranium dioxide, on the other hand, exhibits a minimum in thermal conductivity at around 2000 K. In the vicinity of this stationary point the thermal conductivity of UO_2 does not vary significantly. This minimum is due to
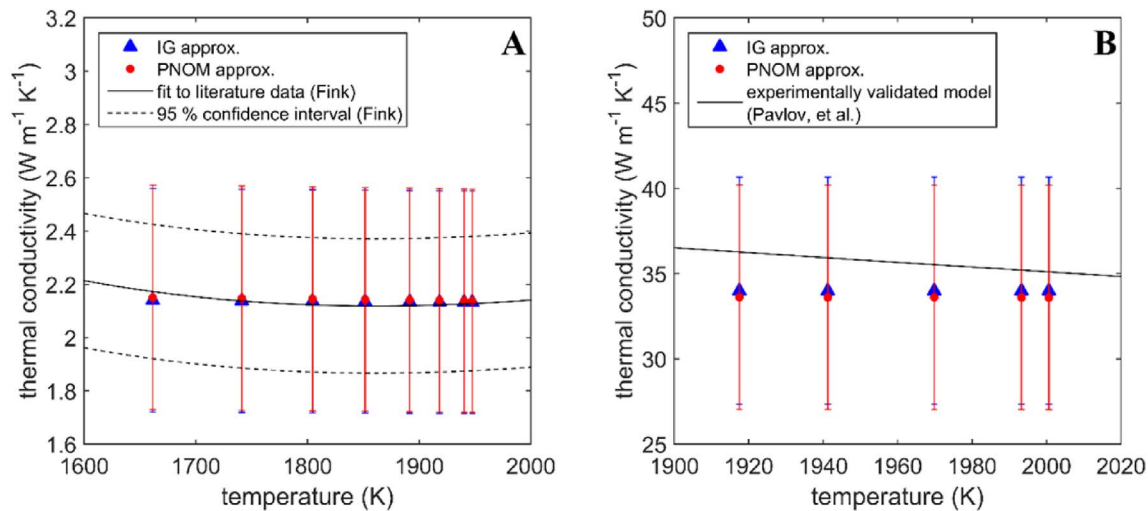
Fig. 8. Experimental evaluation of thermal conductivity of UO$_2$ vs. Temperature (Fig. 8A) Experimentally evaluated thermal conductivity of isostatically pressed graphite vs. Temperature (Fig. 8B). Both properties have been compared to the available literature. The thermal conductivity for each material was evaluated with both the IG approximation and the PNOM approximation. Error bars correspond to two standard deviations combined relative error.

the competition between: 1) degradation of lattice thermal conductivity and 2) increasing electronic thermal conductivity due to mobilisation of electrons (via small polaron hopping) [3,21].

3.4. Experimental limitations and future work

One of the limiting factors when measuring the temperature response on the rear side of the specimen is the size of source effect inherent to all devises measuring radiance, such as pyrometers or thermal cameras. This implies that the temperature measurement does not occur at a discrete spatial point on the surface but is rather an integral quantity of the spatial response function (point spread function) of the devise and the spatial temperature distribution on the measured surface. This effect is not particularly problematic at the centre of the sample surface (when using the experimental configuration described in this work), where the temperature profile is rather flat and the size of source effect can be considered to be negligible. However, towards the edge of the sample, due to steeper temperature gradients such effects may become significant. Hence, a correction procedure should be devised as part of a future study. Another limitation arose due to a transient power instability in the rear laser (this laser was used for preheating the samples and not for pulsing). With increasing power, random power oscillations became apparent (most likely due to the aging and deterioration of components related to the voltage control). These may have corrupted the transient measurements (thermograms). Hence, a laser with a more stable power output will be used in the future to eliminate this source of uncertainty.

The implementation of the previously suggested improvements will benefit future experimental studies and tests on materials with stronger property variations with respect to temperature. Furthermore, the application of more precise, higher resolution thermal cameras will enable the method to be even more sensitive to property variations and achieve its full theoretical potential. Future work will also include testing the method and the two approximations on radially heterogeneous materials. Finally, with regard to the currently used noise

filtering algorithm, in the future more sophisticated approaches, such as Tikhonov regularisation [22] or Wiener filter based conjugate gradient minimisation [23], could be employed for establishing the optimal filter width.

4. Conclusions

A new inverse method has been developed by coupling a numerical model with a laser flash equipment. The method can evaluate thermal conductivity or specific heat capacity as a function of radius and hence temperature with a single measurement. Two approximations were used for the dependence of each property as a function of radius – a polynomial (PNOM) approximation and an iterative gradient (IG) approximation.

The high correlation between fitting parameter pairs does not make simultaneous parameter determination favourable. The synthetic data tests show that both approximations were capable of yielding very good results. The IG approximation is more universal and less sensitive to the fitting initialisation, while the PNOM approximation is less computationally expensive, however, prone to functional artefacts (such as unphysical minima or maxima) and more dependent on the initial fitting parameters.

The experimental results for thermal conductivity of UO$_2$ and isostatically pressed graphite are in good agreement with literature correlations. This provides further confidence in the proposed methodology and its application to other systems.
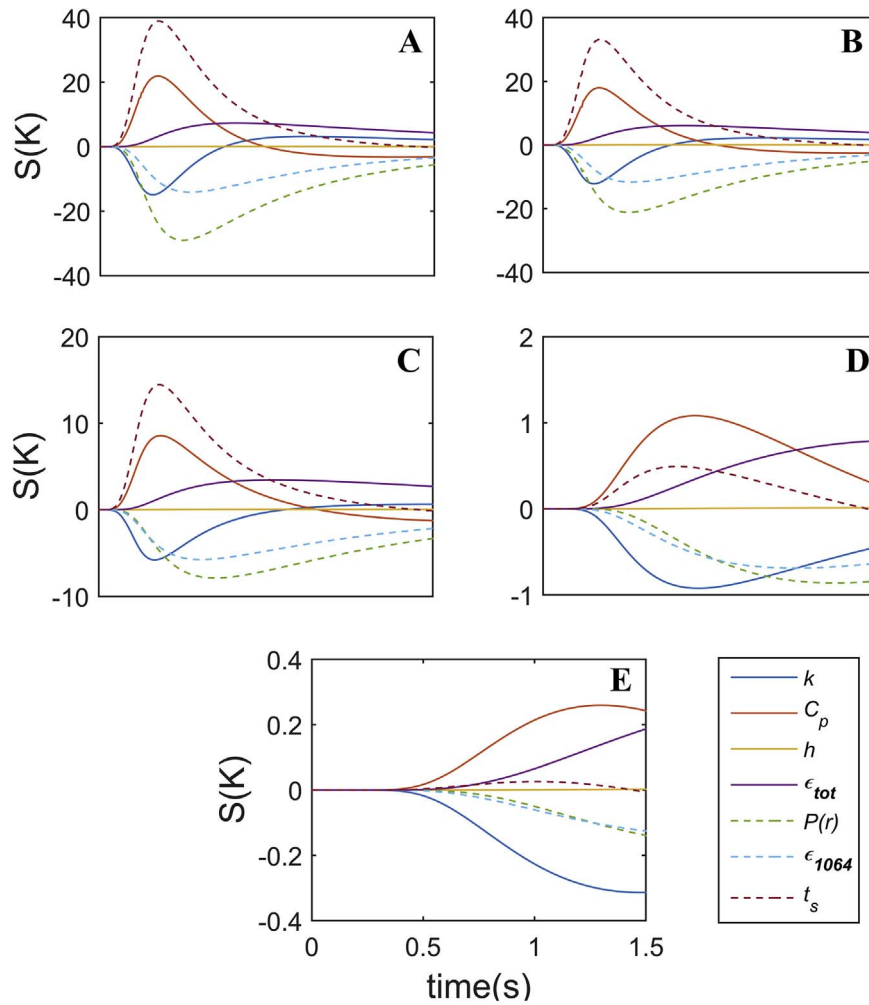
Appendix

Fig. A1. Sensitivity coefficients S (K) on the rear boundary as a function of time computed using the thermo-physical properties of UO$_2$ for various parameters (thermal conductivity (k), specific heat (c_p), convective heat transfer coefficient (h), the total hemispherical emissivity (ε_{tot}), spatial laser beam profile ($P(r)$), absorptivity (ε_{1064}) and thickness (t_s)). A) radial location r = 0; B) radial location r = r$_B$/2; C) radial location r = r$_B$; D) radial location r = r$_B$ + (r$_P$ - r$_B$)/2; E) radial location r = r$_P$; (r$_B$ – beam spot radius (m), r$_P$ – sample radius (m)). The range of each x-axis in each subplot is identical to the one shown in E).

Table A1
Correlation matrix for the four possible fitting parameters at r = 0.

	k	C_p	h	ε
k	1.00	− 0.74	0.11	0.11
C_p	− 0.74	1.00	0.56	0.56
h	0.11	0.56	1.00	1.00
ε	0.11	0.56	1.00	1.00

Table A2
Correlation matrix for the four possible fitting parameters at r = r$_B$/2. (r$_B$ stands for beams spot radius)

	k	C_p	h	ε
k	1.00	− 0.71	0.15	0.14
C_p	− 0.71	1.00	0.55	0.55
h	0.15	0.55	1.00	1.00
ε	0.14	0.55	1.00	1.00

Table A3
Correlation matrix for the four possible fitting parameters at r = r_B. (r_B stands for beams spot radius)

	k	C_p	h	ε
k	1.00	−0.82	−0.14	−0.14
C_p	−0.82	1.00	0.63	0.63
h	−0.14	0.63	1.00	1.00
ε	−0.14	0.63	1.00	1.00

Table A4
Correlation matrix for the four possible fitting parameters at r = r_B + (r_P - r_B)/2. (r_B stands for beams spot radius while r_P stands for pellet radius)

	k	C_p	h	ε
k	1.00	−0.99	−0.75	−0.75
C_p	−0.99	1.00	0.78	0.79
h	−0.75	0.78	1.00	1.00
ε	−0.75	0.79	1.00	1.00

Table A5
Correlation matrix for the four possible fitting parameters at r = r_P. (r_P stands for pellet radius)

	k	C_p	h	ε
k	1.00	−1.00	−0.91	−0.91
C_p	−1.00	1.00	0.87	0.87
h	−0.91	0.87	1.00	1.00
ε	−0.91	0.87	1.00	1.00

$$k(T) = \frac{100}{\left(7.5408 + 17.692*\left(\frac{T}{1000}\right) + 3.6142*\left(\frac{T}{1000}\right)^2\right)} + \frac{6400}{\left(\frac{T}{1000}\right)^{5/2}}*exp\left\{\frac{-16.35}{\left(\frac{T}{1000}\right)}\right\} \tag{A1}$$

where k is thermal conductivity (W m^{-1} K^{-1}) and T is temperature (K).

$$C_P(T) = \left\{ \begin{array}{l} 3.7037*\left[52.1743 + 87.951*\left(\frac{T}{1000}\right) - 84.241*\left(\frac{T}{1000}\right)^2 + \right. \\ \left. + 31.542*\left(\frac{T}{1000}\right)^3 - 2.6334*\left(\frac{T}{1000}\right)^4 - 0.71391*\left(\frac{T}{1000}\right)^{-2} \right] \end{array} \right. \tag{A2}$$

where C_p is specific heat (J kg^{-1} K^{-1}) and T is temperature (K).

References

[1] W.J. Parker, R.J. Jenkins, C.P. Butler, G.L. Abbott, Flash method of determining thermal diffusivity, heat Capacity, and thermal conductivity, J Appl Phys 32 (1961) 1679–1684.

[2] R.D. Cowan, Pulse method of measuring thermal diffusivity at high temperatures, J Appl Phys 34 (1963) 926–927.

[3] C. Ronchi, M. Sheindlin, Thermal conductivity of uranium dioxide up to 2900 K from simultaneous measurement of the heat capacity and thermal diffusivity, J Appl Phys 85 (1999) 776–789.

[4] T. Pavlov, L. Vlahovic, D. Staicu, R.J.M. Konings, M.R. Wenman, P. Van Uffelen, et al., A new numerical method and modified apparatus for the simultaneous evaluation of thermo-physical properties above 1500?K: A case study on iso-statically pressed graphite, Thermochim Acta 652 (2017) 39–52.

[5] F. Cernuschi, A. Russo, L. Lorenzoni, A. Figari, In-plane thermal diffusivity eva-luation by infrared thermography, Rev Sci Instrum 72 (2001) 3988–3995.

[6] J.F. Bisson, D. Fournier, Influence of diffraction on low thermal diffusivity mea-surements with infrared photothermal microscopy, J Appl Phys 83 (1998) 1036–1042.

[7] J.-F. Bisson, D. Fournier, M. Poulain, O. Lavigne, Thermal conductivity of yttria – zirconia single crystals, determined with spatially resolved infrared thermography, J Am Ceram Soc 83 (2000) 1993–1998.

[8] F. Cernuschi, L. Lorenzoni, P. Bianchi, A. Figari, The effects of sample surface

treatments on laser flash thermal diffusivity measurements, Infrared Phys Technol 43 (2002) 133–138.

[9] J. Spino, K. Vennix, M. Coquerelle, Detailed characterisation of the rim micro-structure in PWR fuels in the burn-up range 40-67 GWd/tM, J Nucl Mat. 231 (1996) 179–190.

[10] C. Walker, Assessment of the radial extent and completion of recrystallisation in high burn-up UO2 nuclear fuel by EPMA, J Nucl Mat. 275 (1999) 56–62.

[11] PDE Solutions, FlexPDE, (2013).

[12] J.K. Fink, Thermophysical properties of uranium dioxide, J Nucl Mat. 279 (2000) 1–18.

[13] M. Bober, H.U. Karow, K. Mueller, Study of the spectral reflectivity and emissivity of liquid ceramics, High Temp - High Press 12 (1980) 161–168.

[14] H. Karow, M. Bober, Experimental investigations into the spectral reflectivities and emissivities of liquid UO2, Thermodyn Nucl Mat. 1 (1979).

[15] J.H. Harding, D.G. Martin, P.E. Potter, Thermophysical and thermochemical properties of fast reactor materials, (1989), http://dx.doi.org/10.1177/0193723509343615.

[16] B. Hay, K. Anhalt, L. Chapman, K. Boboridis, J. Hameury, S. Krenek, et al., Traceability improvement of high temperature thermal property measurements of materials for new fission reactors, IEEE Trans Nucl Sci 61 (2014) 2112–2119.

[17] T. Matsumoto, A. Ono, Specific heat capacity and emissivity measurements of ribbon-shaped graphite using pulse current heating, Int J Thermophys 16 (1995) 267–275.

[18] D. Marquardt, An algorithm for least-squares estimation of nonlinear parameters, J

Soc Ind Appl Math 11 (1963) 431–441.

[19] J. Moore, The levenberg marquardt method implementation and theory, Conference on numevical analysis, 1977, pp. 1–12.

[20] R. Brandt, G. Neuer, Thermal conductivity and thermal radiation properties of UO2, J Non-Equilibrium Thermodyn 1 (1976) 3–23.

[21] T. Pavlov, M.R. Wenman, L. Vlahovic, D. Robba, R.J.M. Konings, P. Van Uffelen, et al., Measurement and interpretation of the thermo-physical properties of UO2 at high temperatures: the viral effect of oxygen defects, Acta Mat 139 (2017) 138–154.

[22] K.A. Woodbury, J.V. Beck, Estimation metrics and optimal regularization in a Tikhonov digital filter for the inverse heat conduction problem, Int J Heat Mass Transf 62 (2013) 31–39.

[23] F. Bozzoli, S. Rainieri, Comparative application of CGM and Wiener filtering techniques for the estimation of heat flux distribution, Inverse Probl Sci Eng 19 (2011) 551–573.